Nano Research

ISSN 1998-0124 CN 11-5974/O4
https://doi.org/10.1007/s12274-020-3142-9

Research Article

High power and stable P-doped yolk–shell structured Si@C anode simultaneously enhancing conductivity and Li^+ diffusion kinetics

Ming Chen[1], Qinnan Zhou[1], Jiantao Zai[1] (✉), Asma Iqbal[1], TsegayeTadesse Tsega[1], Boxu Dong[1], Xuejiao Liu[1], Yuchi Zhang[1], Changyu Yan[1], Liang Zhao[1], Ali Nazakat[1], SharelPeisan E[2,3], CheeTongJohn Low[2] (✉), and Xuefeng Qian[1] (✉)

[1] *Shanghai Electrochemical Energy Devices Research Center, School of Chemistry and Chemical Engineering and State Key Laboratory of Metal Matrix Composites, Shanghai Jiao Tong University, Shanghai 200240, China*
[2] *Warwick Electrochemical Engineering Group, WMG, Energy Innovation Centre, University of Warwick, CV4 7AL, UK*
[3] *School of Health & Life Sciences, Teesside University, Middlesbrough, TS1 3BX, UK*

Received: 13 August 2020 / **Revised:** 21 September 2020 / **Accepted:** 23 September 2020

ABSTRACT

Silicon is a low price and high capacity anode material for lithium-ion batteries. The yolk–shell structure can effectively accommodate Si expansion to improve stability. However, the limited rate performance of Si anodes can't meet people's growing demand for high power density. Herein, the phosphorus-doped yolk–shell Si@C materials (P-doped Si@C) were prepared through carbon coating on P-doped Si/SiO_x matrix to obtain high power and stable devices. Therefore, the as-prepared P-doped Si@C electrodes delivered a rapid increase in Coulombic efficiency from 74.4% to 99.6% after only 6 cycles, high capacity retention of ~ 95% over 800 cycles at 4 $A{\cdot}g^{-1}$, and great rate capability (510 $mAh{\cdot}g^{-1}$ at 35 $A{\cdot}g^{-1}$). As a result, P-doped Si@C anodes paired with commercial activated carbon and $LiFePO_4$ cathode to assemble lithium-ion capacitor (high power density of ~ 61,080 $W{\cdot}kg^{-1}$ at 20 $A{\cdot}g^{-1}$) and lithium-ion full cell (good rate performance with 68.3 $mAh{\cdot}g^{-1}$ at 5 C), respectively. This work can provide an effective way to further improve power density and stability for energy storage devices.

KEYWORDS

P-doped yolk–shell structured Si@C anode, excellent rate performance, long life, lithium-ion battery, high power, full cell

1 Introduction

Lithium-ion battery (LIB) featuring high capacity, light weight and long life, is an significant energy storage device [1–4]. Many materials (such as Li metal [5, 6], Si [7], $SnSe_x$ [8], Mn_3O_4 [9], ReS_2 [10]) can be used as the negative electrodes of LIBs. Li metal anode has been extensively studied owing to the high theoretical capacity, low density, and low redox potential [11]. But, the growth of Li dendrites can cause serious safety problems to hinder practical application. At present, the commercial graphite anode of LIB shows excellent electrical conductivity and long cycle stability. However, its low capacity (372 $mAh{\cdot}g^{-1}$) can't meet the increasing demands of high energy and power densities [12–14].

Si is a high theoretical capacity (4,200 $mAh{\cdot}g^{-1}$), rich in the crust, and low price anode material for LIBs [15–20]. However, the huge volume expansion (~ 300%) of Si materials can bring about pulverization of active materials to seriously hinder its practical applications as given in Fig. 1(a) [21–25]. The design of yolk–shell Si-C can ease the problem of bulk expansion to improve electrochemical lithium storage performance [26–32]. Cui group [26] reported the yolk–shell structured Si-C materials (using silicon nanoparticles as the yolk and carbonized dopamine as the carbon layer) achieved good electrochemical performance for LIB. Unfortunately, the intrinsic semiconductor property of silicon is often not considered in the published work [33–35]. For the yolk–shell structure, the low electron conductivity of intrinsic Si nanoparticles (SiNPs) as yolk impeded the rapid transmission of electrons between the inside interconnected SiNPs and the outside carbon layer as shell, resulting in low conductivity and slow electron transfer in the yolk–shell Si@C electrode (Fig. 1(b)), which suffered from low Coulombic efficiency and poor rate performance for LIBs. Compared with boron doping, phosphorus element as an electron donor is doped in silicon materials to be more conducive to improving electronic conductivity.[21, 36, 37]

With this in mind, P-doping concept was introduced in this research to improve electron transfer of yolk–shell structured Si@C electrode. The P-doped yolk–shell structured Si@C (P-doped Si@C) was prepared by pyrolysis of C_2H_2 on P-doped Si/SiO_2 composite through adding the P_2O_5 to process of the SiO thermal disproportionation and subsequently SiO_2 etching. Thanks to enhancing whole electrical conductivity, Li^+ diffusivity in electrode materials, and keeping the structural integrity as presented in Fig. 1(c), the obtained P-doped Si@C electrodes achieved a Coulombic efficiency of up to 99.6% through only six cycles and high reversible capacity of 1,005 $mAh{\cdot}g^{-1}$ (high capacity retention of ~ 95%) at 4 $A{\cdot}g^{-1}$ after 800 cycles. In addition, the P-doped Si@C electrode also showed excellent rate capability (510 $mAh{\cdot}g^{-1}$ at 35 $A{\cdot}g^{-1}$). The P-doped Si@C anode

Address correspondence to Jiantao Zai, zaijiantao@sjtu.edu.cn; CheeTongJohn Low, C.T.J.Low@warwick.ac.uk; Xuefeng Qian, xfqian@sjtu.edu.cn

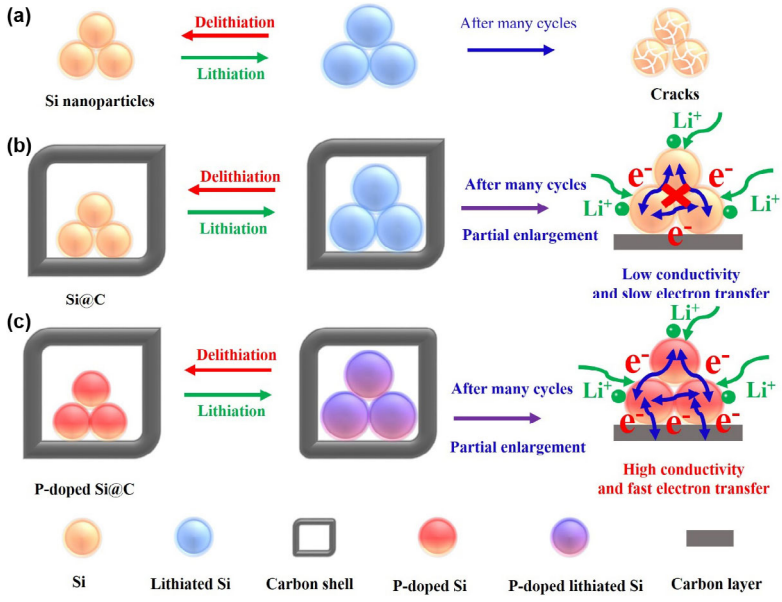

Figure 1 Schematic illustration of Li^+ insertion/extraction in SiNPs, Si@C, and P-doped Si@C electrodes: (a) SiNPs suffering from the much larger resistance and volume expansion after many cycles; (b) yolk–shell Si@C suffering from low conductivity and slow electron transfer in the yolk; (c) P-doped Si@C electrode possessing high conductivity and fast electron transfer in the yolk.

matched commercial activated carbon cathode for lithium-ion capacitor (LIC), which delivered an energy density of 51 $Wh{\cdot}kg^{-1}$ at the high-power density of ~ 61,080 $W{\cdot}kg^{-1}$. When paired with commercial $LiFePO_4$ cathode, lithium-ion full cell showed great rate performance (68.3 $mAh{\cdot}g^{-1}$ at 5 C).

2 Experimental

2.1 Material synthesis

Silicon monoxide microparticles (SiO MPs, ~ 5 μm) and P_2O_5 powder (the weight ratio was 10:1) were mixed uniformly and heated to 950 °C for 5 h under argon. The disproportionation of SiO generated Si nanoparticles buried at SiO_2 matrix. At the same time the interconnected SiNPs were also uniformly doped by P_2O_5. For the bare SiNPs without P-doping directly were obtained by HF eching. The P-doped Si@C material was obtained through carbon layer coated on the surface of P-doped Si from thermal decomposition of C_2H_2:Ar (1:9 by volume) at a flow rate of 0.15 $L{\cdot}min^{-1}$ at 800 °C for 10 min after washing with 10 wt.% HF solution. For comparison, except for the samples without P_2O_5, other experimental conditions were the same to prepare yolk–shell Si@C.

2.2 Preparation of electrodes and cell assembly

The P-doped Si@C electrode was prepared by mixing in a weight ratio of active material:acetylene black:poly(acrylic acid) = 7:1.5:1.5 on Cu foil. The commercial activated carbon (AC) and $LiFePO_4$ cathodes were prepared by mixing in a ratio of active material:acetylene black:cellulose sodium = 8:1:1 on Al foil. Subsequently, these electrodes were dried in vacuum at 80 °C for 12 h. In addition, P-doped Si@C anode paired with commercial activated carbon and $LiFePO_4$ cathodes to assemble P-doped Si@C||AC LIC and P-doped Si@C/$LiFePO_4$ full cells. The active mass loading of P-doped Si@C anode and cathodes (commercial activated carbon or $LiFePO_4$) were about 0.8 and 4.8 $mg{\cdot}cm^{-2}$ by a weight ratio of anode and cathode = 1:6 (the amount of electrolyte was about 100 μL), respectively. The coin cells (CR2016) were assembled in a glove box filled with high purity argon using polypropylene membrane as separator and 1 M $LiPF_6$ in a mixture of ethylene carbonate:dimethyl carbonate (v:v =1:1) and 10 wt.% fluoroethylene carbonate as electrolyte. The galvanostatic charge and discharge experiments were performed on a battery tester LAND-CT2001A in the voltage windows of 0.01–1.5 and 2–4 V at room temperature. The energy density (E) and power density (P) were calculated by using following equations.

$$E = \int_{t_0}^{t_1} VI\mathrm{d}t$$

where V is the voltage, I is the constant current density, and t_0 and t_1 are starting and ending time of discharge, respectively.

$$P = E / t$$

where t is time of discharge.

2.3 Characterizations and electrochemical measurements

The morphology of samples was observed using a NOVA Nano SEM 230 field-emission scanning electron microscope (FEI, USA). The microstructure structure of samples was characterized using a JEM-2100F TEM (JEOL, Japan) operating at 200 kV. X-ray diffraction (XRD) patterns were recorded on a D/max 2550VL/PC X-ray diffractometer (Rigaku, Japan) equipped with Cu Kα radiation (λ = 1.5418 Å, 40 kV, 30 mA). Raman spectra were acquired using an in Via-reflex micro-Raman spectrometer (Renishaw, UK) with a 532 nm wavelength incident laser. Thermogravimetric analysis (TGA) was performance on a SDT Q600 thermoanalyzer (DSC-TGA, TA, USA) in air. X-ray photoelectron spectroscopy (XPS) was carried out on an AXIS Ultra DLD spectrometer (Kratos, Japan) with Al Kα radiation (hv = 1,486.6 eV). The specific surface area and pore size distribution of materials were measured using a NOVA2200e analyzer (Quantachrome, USA). Cyclic voltammetry (CV), the conductivity (I–V) and electrochemical impedance spectrum (EIS) were measured on a ZAHNER Zennium electrochemical workstation.

3 Results and discussion

Figure 2 display the fabrication process of the P-doped Si@C material. The SiO (Fig. S1 in the Electronic Supplementary

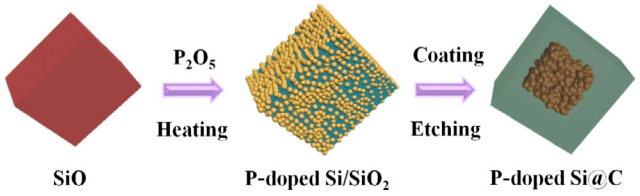

Figure 2 The fabrication procedure of P-doped Si@C material.

Material (ESM)) and P_2O_5 were employed as Si and P sources, respectively. Then, the above mixture was heated to make SiO thermal disproportionation and P doping simultaneously to form P-doped Si/SiO_2 composite (Fig. S2 in the ESM). Subsequently, the P-doped Si/SiO_2@C (Fig. S3 in the ESM) was prepared by pyrolysis of C_2H_2 on above composite. Finally, yolk–shell P-doped Si@C material with interconnected P-doped Si yolk and carbon shell was obtained after HF etching.

The scanning electron microscopy (SEM) image of the P-doped Si@C sample (Fig. 3(a)) shows a microscale yolk–shell Si-C structure. It is obvious from the transmission electron microscopy (TEM) images that the interconnected Si nanoparticles as yolk are totally encapsulated by carbon shell as presented in Figs. 3(b) and 3(c). The thickness of carbon shell having amorphous nature is about 10 nm as seen in the TEM image (Fig. 3(d)). Moreover, the high-resolution TEM (HRTEM) image (Fig. 3(e)) can be clearly seen lattice fringes of Si (111) with spacing of 0.32 nm [34, 38]. The successfull doping with uniform distribution of P element (the P content is 2.03 at.%) in the interconnected Si nanoparticles was evident from the elemental mapping analysis (Fig. 3(f)).

Furthermore, XRD, Raman and XPS were used to confirm P-doping in the yolk–shell Si@C sample. Figure 4(a) presents

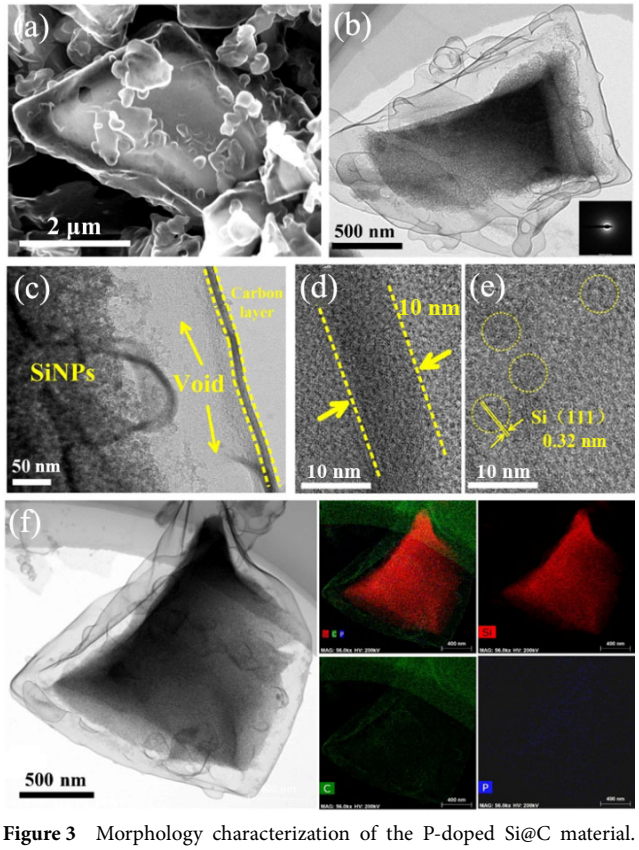

Figure 3 Morphology characterization of the P-doped Si@C material. (a) SEM image. (b) TEM image (the inset: selected area electron diffraction (SAED) image). (c) Magnified TEM image. (d) and (e) HRTEM images, and (f) TEM image and elemental mapping (colour scheme: Si, red; C, green; P, blue).

XRD patterns of SiNP (images of TEM in Fig. S4 in the ESM), Si@C (images of SEM and TEM in Fig. S5 in the ESM), and P-doped Si@C with unobvious peak of amorphous carbon [39, 40]. A shift towards small angle is observed in diffraction peaks for P-doped Si@C particles, whereas the diffraction peaks of (111) altered to be blunt by P doping. This could be ascribed to impurity incorporation (P-doping), resulting in part Si atoms replaced by P atoms increasing the disorder of lattice in Si [36, 41]. The porous structure of P-doped Si@C sample was further verified by nitrogen adsorption–desorption isotherm type IV curves (Fig. 4(b)). The specific surface area of P-doped Si@C material was 307.4 $m^2 \cdot g^{-1}$. From the inset of Fig. 4(b), it can be seen that the pore size distribution is mainly centered at 5–10 nm, revealing its mesoporous structure. The Raman spectrum of the P-doped Si@C sample (Fig. 4(c)) exhibited an shift of Si reference peak from 518 to 504 cm^{-1}. It is well known that P doping in the Si can decrease the mean free path and lifetime of phonon [41–43]. The distinct peaks at 1,334.5 and 1,593.6 cm^{-1} of the P-doped Si@C sample were attribute to D and G bands of the amorphous carbon (carbon content is about 10.1% in Fig. S6 in the ESM), respectively [26, 40]. The XPS analysis was also carried out to find phosphorus bonding within interconnected SiNPs in Fig. 4(d). The Si 2p spectra of P-doped Si@C sample showed peaks for SiO2, Si–Si and n-type Si at 103.2, 99.6, and 100.0 eV, respectively. To further provide evidence of P doping, Si–P and P–P bonds at 128.9 and 130.5 eV can be found from the P 2p XPS spectrum of P-doped Si@C sample in Fig. 4(e) [37, 41, 44, 45]. Moreover, P 2s XPS spectrum as given in Fig. 4(f) also examined Si 2s plasmon loss signal [46].

To explore the effect of different P doping levels on lithium storage performance, the L-P-doped Si@C (P content of 1.19 at.% in Fig. S7 in the ESM) and H-P-doped Si@C (P content of 4.00 at.% in Fig. S8 in the ESM) materials were prepared by mixing SiO and P2O5 powders (weight ratio 20:1 and 5:1) in process of disproportionation reaction, respectively. Figure S9 in the ESM presents the cycling performance of three samples with different weight ratios (20:1, 10:1 and 5:1) at current density of 1 $A \cdot g^{-1}$. However, the L-P-doped Si@C electrode showed worse cycling stability and H-P-doped Si@C electrode delivered lower capacity. The low P-doping amount may cause less reactive sites and low conductivity, while high levels of phosphorus may replace more silicon atoms, resulting in lower capacity for electrochemical lithium storage [21, 41, 47].

CV plot of the first three cycles of P-doped Si@C electrode is displayed in Fig. S10 in the ESM at 0.5 $mV \cdot s^{-1}$. The CV curves has a good coincidence, indicating excellent reversibility of P-doped Si@C electrode [48, 49]. The first charge and discharge curves of the SiNP, Si@C and P-doped Si@C electrodes at 0.4 $A \cdot g^{-1}$ are shown in Fig. 5(a). SiNP, Si@C, and P-doped Si@C electrodes show the initial discharge capacities of 2,906, 2,646 and 2,847 $mAh \cdot g^{-1}$ (corresponding initial Coulombic efficiencies (ICEs) are 54.2%, 67.7% and 74.4%, respectively). Among these electrodes, P-doped Si@C electrode shows the highest ICE (74.4%). the carbon shell of P-doped Si@C may prevent most of the electrolyte from infiltrating inside porous silicon nanoparticles to form less solid electrolyte interphase (SEI) and the doping of P effectively improves the electron conductivity to get higher reversible capacity. While, the ICE of SiNP electrode is only 54.2%, due to more SEI on the surfaces of silicon nanoparticles from larger specific surface [40, 50, 51]. The obtained P-doped Si@C electrode achieved a Coulombic efficiency of up to 99.6% through only six cycles as displayed in Fig. 5(b). However, the SiNP and Si@C anodes could not approach 99.5% stabilized efficiency even after 12 cycles. The

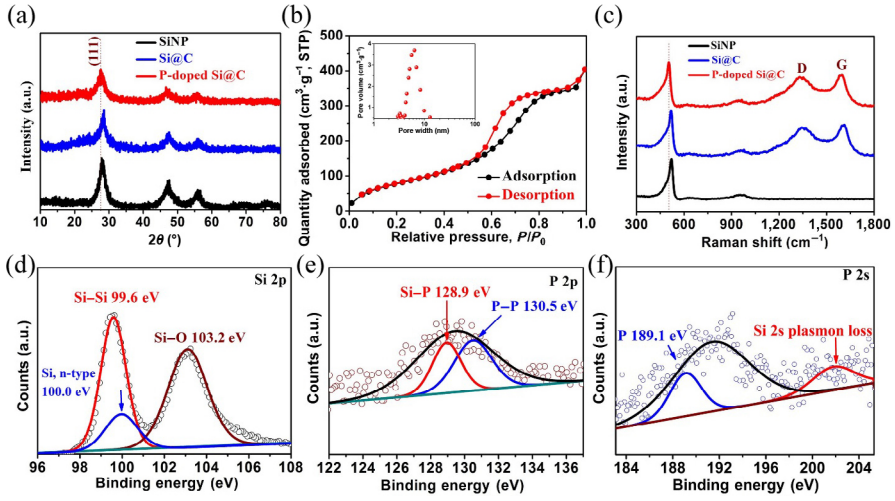

Figure 4 Characterization of the prepared SiNP, Si@C and P-doped Si@C samples. (a) XRD patterns of SiNP, Si@C and P-doped Si@C samples. (b) Nitrogen adsorption–desorption isotherm curves of P-doped Si@C sample (pore diameter distribution in the inset). (c) Raman spectra of SiNP, Si@C and P-doped Si@C samples. XPS spectra of the P-doped Si@C sample for (d) Si 2p, (e) P 2p and (f) P 2s.

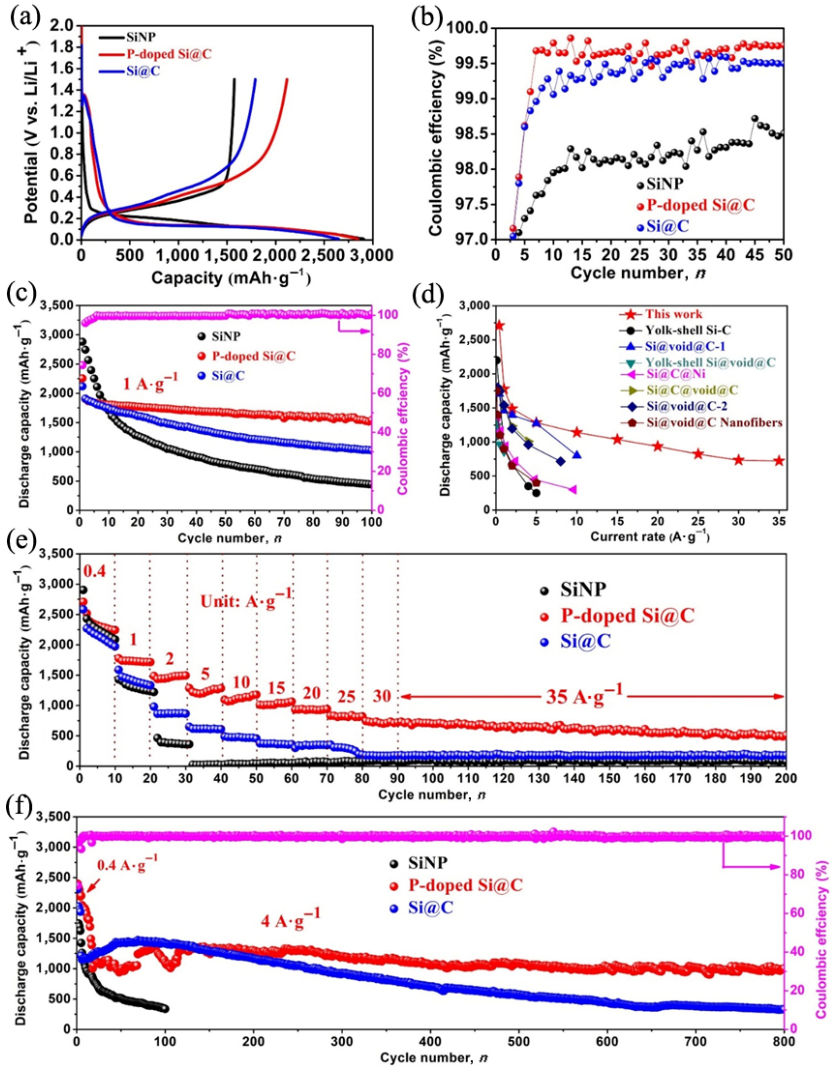

Figure 5 Electrochemical properties of the prepared SiNP, Si@C and P-doped Si@C electrodes. (a) The intial discharge/charge curves. (b) Magnified form of stabilized Coulombic efficiency for SiNP, Si@C and P-doped Si@C electrodes at 1 A·g^{-1} at first 50 cycles. (c) Cycling performance at 1 A·g^{-1}. (d) Comparison of capacity at different rates for P-doped Si@C with those of reported Si/C yolk–shell nanocomposite anodes [28, 29, 32, 52–55]. (e) Rate capability. (f) Long cycle performance at 4 A·g^{-1} (the first three cycles at 0.4 A·g^{-1}).

P-doped Si@C electrode delivered great cycling stability and high discharge capacity of 1,650 mAh·g^{-1} at the current density of 1 A·g^{-1} after 100 cycles, while SiNP and Si@C electrodes showed rapid capacity fading as given in Fig. 5(c). It is also evident from Fig. 5(d), the P-doped Si@C electrode showed the best rate capability than reported Si-based materials in Refs.

[28, 29, 32, 52–55]. The reversible capacities of P-doped Si@C electrode were 2,709, 1,779, 1,487, 1,284, 1,140, 1,037, 934, 822, 733 and 722 mAh·g^{-1} at different current densities of 0.4, 1, 2, 5, 10, 15, 20, 25, 30 and 35 A·g^{-1} in Fig. 5(e), respectively. It was noticed that P-doped Si@C electrode showed excellent cycle stability and high capacity of 510 mAh·g^{-1} at up to current density of 35 A·g^{-1} (the charging and discharging curves of P-doped Si@C electrode in Fig. S11 in the ESM), while SiNP and Si@C anodes exhibited rapid decay, indicating poor rate performance. Figure 5(f) shows the long cycling performance of SiNP, Si@C and P-doped Si@C electrodes at 4 A·g^{-1} after activation at 0.4 A·g^{-1}. The P-doped Si@C electrode displayed a high reversible capacities of 1,005 mAh·g^{-1} at 4 A·g^{-1} after 800 cycles, corresponding to a retention of about 95% to its initial value of 1,056 mAh·g^{-1} at 4 A·g^{-1}. While Si@C electrode only delivered discharge capacities of less than 330 mAh·g^{-1}, corresponding to a retention of about 27.7%.

The P-doped Si@C electrode demonstrated high electrical conductivity and kept intact yolk–shell structure, resulting in excellent electrochemical lithium storage performances. Figure 6(a) shows *I*–*V* curves of SiNP, Si@C and P-doped Si@C powder samples at scan rate of 10 mV·s^{-1}. From Table S1 in the ESM, one can see the P-doped Si@C powder sample (9.8×10^{-4} S·m^{-1}) presented the higher conductivity than Si@C (1.7×10^{-4} S·m^{-1}) and SiNP (6.5×10^{-6} S·m^{-1}) powder samples [30, 34, 56]. The EIS can be conducive to understanding P doping to enhance reaction kinetics of Si@C electrode. The Nyquist plot in Fig. 6(b) shows one semicircle in high-frequency region and an inclined line in low-frequency region, corresponding to the resistance from surface film (R_f is total resistance of the carbon layer and SEI), charge transfer resistance (R_{ct}), and the Warburg impedance (W represents Li^+ diffusion in electrode), respectively [57]. As shown in Fig. 6(b), P-doped Si@C electrode displayed the smallest semicircle than SiNP and Si@C electrodes, implying smallest charge transfer resistance derived from the P doping enhancing conductivity. The Warburg impedance in the low frequency region (Fig. 6(c)) indicates the Li^+ diffusion coefficient of P-doped Si@C electrode, showing highest Li^+ diffusion coefficient (D_{Li^+}) of 1.20×10^{-10} cm^2·s^{-1} calculated by Eqs. (1) and (2) [58]. which is much higher than that of the SiNP electrode (9.20×10^{-12} cm^2·s^{-1}) and Si@C electrode (4.42×10^{-11} cm^2·s^{-1}) in Table 1 because P-doping might make the SiNP more lithium storage sites during cycling, resulting in super fast ion transport kinetics [59]. This result proves positive effect of P-doped Si on the Li^+ diffusion for enhancing the rate performance.

$$Z_r = R_s + R_f + R_{ct} + \sigma_w \cdot \omega^{-0.5} \quad (1)$$

$$D_{Li^+} = 0.5(RT/nAF^2\,\sigma_w)^2 \quad (2)$$

where *R*, *T*, and *F* are the constant, *n* is Li^+ concentration, *A* is electrode area, and σ_w is the Warburg factor, R_s, R_f and R_{ct} are series resistance, resistance of surface film, and resistance of charge transfer, respectively.

The cross-sectional SEM images in Figs. 6(b)–6(e) show only 15.4% change for thickness of P-doped Si@C after 50 cycles, demonstrating effectively mitigating large volume changes. Additionally, no obvious morphological and structure differences (SEM images of P-doped Si@C electrode in Fig. S12 in the ESM) of P-doped Si@C electrode were found after 50 cycles as given in Figs. 6(f) and 6(g).

The excellent performances of the P-doped Si@C electrode in Coulombic efficiencies, stability, and rate performance may be attributed to the following reasons: (1) P-doping significantly enhances the conductivity of SiNPs. P-doped interconnected SiNPs as yolk not only improve electrical contact inside

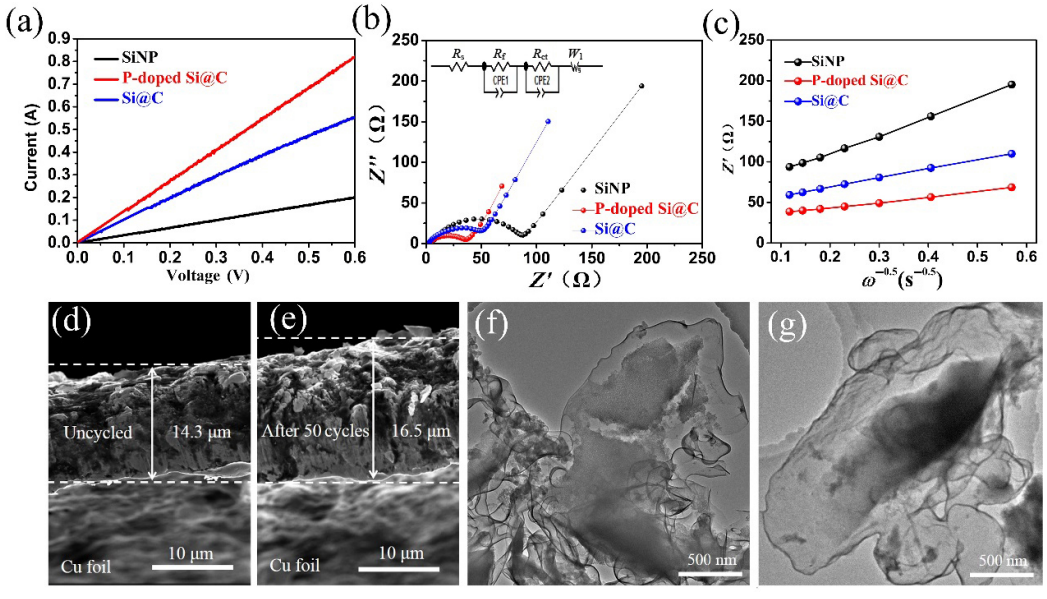

Figure 6 (a) *I*–*V* curves of SiNP, Si@C and P-doped Si@C powder samples. (b) Electrochemical impedance spectra (the inset is the corresponding equivalent circuit) and (c) the relationship between *Z*' and $\omega^{-0.5}$ of SiNP, Si@C and P-doped Si@C electrodes in the low frequency range. (d)–(g) Morphology characterization of P-doped Si@C electrode: SEM images of (d) uncycled and (e) after 50 cycles; TEM images of (f) unclycled and (g) after 50 cycles.

Table 1 Kinetic parameters of SiNP, Si@C and P-doped Si@C electrodes

Electrodes	R_s (Ω)	R_f (Ω)	R_{ct} (Ω)	σ_w (Ω·s$^{-0.5}$)	D_{Li^+} (cm^2·s^{-1})
SiNP	3.27	1.86	64.72	62.08	9.20×10^{-12}
P-doped Si@C	3.15	2.10	26.75	17.19	1.20×10^{-10}
Si@C	3.25	2.25	44.57	28.97	4.42×10^{-11}

interconnected SiNPs, but also facilitate the electron transfer between SiNPs and carbon layers, which is in favor of high electron conductivity, fast Li^+ storage kinetics and utilization ratio [21, 41, 45]. (2) The yolk–shell structured inner void can accommodate Si expansion during cycling. (3) The outside carbon shell of P-doped interconnected SiNPs keep structural integrity and enhance the conductivity throughout the electrode to enhance the electrochemical kinetics. In addition, the carbn coating layer contributes to stable SEI formation on surface [26, 40].

The P-doped Si@C electrode exhibited remarkable rate performance for LIBs, showing great potential for LICs, which were assembled by P-doped Si@C anode and commercial AC (the SEM images in Fig. S13 in the ESM) cathode as given in Fig. 7(a). It is observed that the CV curves of P-doped Si@C||AC LIC show a rectangle-like shape at different scan rates. Even if the sweep speed increases by 20 $mV·s^{-1}$, the shape is basically unchanged, indicating noticeable power capability for LIC (Fig. 7(b)). Figure 7(d) displays the voltage profiles from current densities of 1 to 20 $A·g^{-1}$ (voltage window: 2.0–4.0 V). These curves are different from triangle and linear shape, suggesting storage characteristics both battery and capacitor [60]. The P-doped Si@C||AC LIC delivered an high energy density of ~ 200 $Wh·kg^{-1}$ calculated by the mass of commercial AC at 2.5 $A·g^{-1}$ after 500 cycles, equivalent to four times that of lithium foil||AC LIC full cell shown in Fig. 7(c). As shown in Fig. 7(e), the energy densities calculated by the mass of commercial AC of P-doped Si@C||AC LIC were 220, 207, 150, 105, 83, and 61 $Wh·kg^{-1}$ at the current densities of 1, 2, 5, 10, 15, and 20 $A·g^{-1}$, respectively. However, the energy density of lithium foil||AC LIC was almost zero at 20 $A·g^{-1}$. Compared to variously reported Si-based LICs, our work is among the highest level in Fig. 7(f) [61–64]. The high energy density of ~ 189 $Wh·kg^{-1}$ of the P-doped Si@C||AC LIC was achieved at the power density of ~ 10,174 $W·kg^{-1}$. The LIC showed an energy density of 51 $Wh·kg^{-1}$ at the maximum power density of ~ 61,080 $W·kg^{-1}$ (at 20 $A·g^{-1}$) calculated by the mass of P-doped Si@C and AC, due to excellent electrical performances of P-doped Si@C material. In addition, we also explored its commercial viability by fabricating a P-doped Si@C/$LiFePO_4$ full cell (P-doped Si@C anode and $LiFePO_4$ cathode (electrochemical performances in Fig. S14 in the ESM)), which delivered 68.3 $mAh·g^{-1}$ at 5 C and 92 $mAh·g^{-1}$ at 1 C = 170 $mA·g^{-1}$ after 200 cycles as given in Fig. S15 in the ESM.

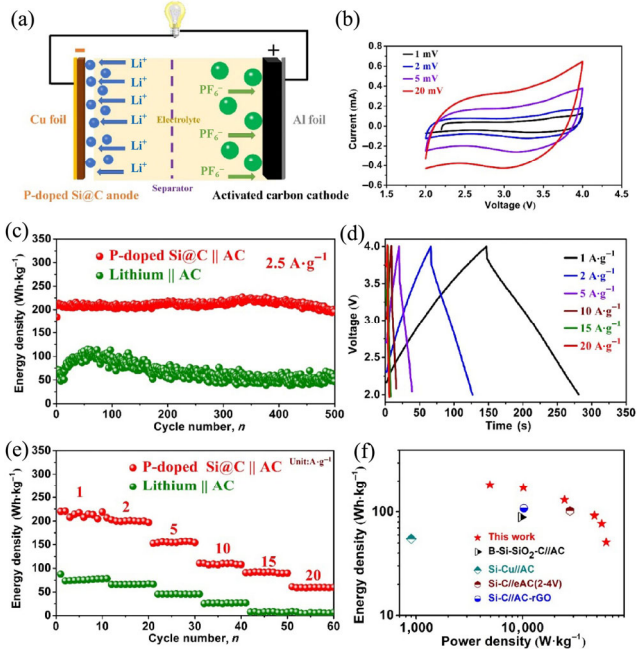

Figure 7 (a) Schematic illustration of LIC containing P-doped Si@C anode and AC cathode. (b) CV curves of P-doped Si@C||AC LIC at different scan rates. (c) Cycling performance of P-doped Si@C||AC LIC and lithium foil||AC LIC (the mass ratio of P-doped Si@C to AC is 1:6 and energy density is calculated by the mass of activated carbon) at 2.5 $A·g^{-1}$. (d) Voltage profiles of P-doped Si@C||AC LIC at various current densities. (e) Rate performances of P-doped Si@C||AC LIC and lithium foil||AC LIC (energy density is calculated by the mass of activated carbon). (f) Ragone plot of P-doped Si@C||AC LIC compared to Si-based LICs in Refs. [61–64] (energy density is calculated by the total mass of P-doped Si@C and activated carbon).

4 Conclusion

In summary, the P-doped yolk–shell structured Si@C was prepared through pyrolysis of C_2H_2 on P-doped Si/SiO_2 composite from SiO thermal disproportionation. This rational strategy of P-doping, effectively improved fast electron transfer and enhanced reaction kinetics for yolk–shell Si@C electrode, achieving excellent lithium storage performances (1,005 $mAh·g^{-1}$ at 4 $A·g^{-1}$ after 800 cycles and 510 $mAh·g^{-1}$ at 35 $A·g^{-1}$). Therefore, the P-doped Si@C anode was successfully applied in high power lithium ion capacitor (high-power density of ~ 61,080 $W·kg^{-1}$ at 20 $A·g^{-1}$) and excellent rate performance lithium-ion full cell (68.3 $mAh·g^{-1}$ at 5 C). The approach presented in the research could be universal to help improve poor conductivity and low reaction kinetics for advanced anode materials in lithium-ion batteries.

Acknowledgements

The work is supported by Science and Technology Commission of Shanghai Municipality (Nos. 20520710400, 18230743400 and 18QA1402400), the National Natural Science Foundation of China (No. 21771124), Oceanic Interdisciplinary Program of Shanghai Jiao Tong University (No. SL2020MS020), and SJTU-Warwick Joint Seed Fund (2019/20).

Electronic Supplementary Material: Supplementary material (SEM, TEM, XRD of materials, and electrochemical performances of different P content electrodes and P-doped Si@C/$LiFePO_4$ full cells) is available in the online version of this article at https://doi.org/10.1007/s12274-020-3142-9.

References

[1] Aricò, A. S.; Bruce, P.; Scrosati, B.; Tarascon, J. M.; van Schalkwijk, W. Nanostructured materials for advanced energy conversion and storage devices. *Nat. Mater.* **2005**, *4*, 366–377.

[2] Armand, M.; Tarascon, J. M. Building better batteries. *Nature* **2008**, *451*, 652–657.

[3] Dunn, B.; Kamath, H.; Tarascon, J. M. Electrical energy storage for the grid: A battery of choices. *Science* **2011**, *334*, 928–935.

[4] Yi, Z.; Wang, W. W.; Qian, Y.; Liu, X. Y.; Lin, N.; Qian, Y. T. Mechanical pressing route for scalable preparation of microstructured/nanostrutured Si/graphite composite for lithium ion battery anodes. *ACS Sustainable Chem. Eng.* **2018**, *6*, 14230–14238.

[5] Gurung, A.; Pokharel, J.; Baniya, A.; Pathak, R.; Chen, K.; Lamsal, B. S.; Ghimire, N.; Zhang, W. H.; Zhou, Y.; Qiao, Q. Q. A review on strategies addressing interface incompatibilities in inorganic all-solid-state lithium batteries. *Sustainable Energy Fuels* **2019**, *3*, 3279– 3309.

[6] Chen, K.; Pathak, R.; Gurung, A.; Reza, K. M.; Ghimire, N.; Pokharel, J.; Baniya, A.; He, W.; Wu, J. J.; Qiao, Q. Q. et al. A copper-clad lithiophilic current collector for dendrite-free lithium metal anodes. *J. Mater. Chem. A* **2020**, *8*, 1911–1919.

[7] McGraw, M.; Kolla, P.; Yao, B.; Cook, R.; Quiao, Q.; Wu, J.; Smirnova, A. One-step solid-state *in-situ* thermal polymerization of silicon-PEDOT nanocomposites for the application in lithium-ion battery anodes. *Polymer* **2016**, *99*, 488–495.

[8] Gurung, A.; Naderi, R.; Vaagensmith, B.; Varnekar, G.; Zhou, Z. P.; Elbohy, H.; Qiao, Q. Q. Tin selenide—Multi-walled carbon nanotubes hybrid anodes for high performance lithium-ion batteries. *Electrochim. Acta* **2016**, *211*, 720–725.

[9] Varapragasam, S. J. P.; Balasanthiran, C.; Gurung, A.; Qiao, Q. Q.; Rioux, R. M.; Hoefelmeyer, J. D. Kirkendall growth of hollow Mn_3O_4 nanoparticles upon galvanic reaction of MnO with Cu^{2+} and evaluation as anode for lithium-ion batteries. *J. Phys. Chem. C* **2017**, *121*, 11089–11099.

[10] Liu, S.; Lei, W. W.; Liu, Y.; Qiao, Q. Q.; Zhang, W. H. Hierarchical nanosheet-based MS_2 (M = Re, Mo, W) nanotubes prepared by templating sacrificial Te nanowires with superior lithium and sodium storage capacity. *ACS Appl. Mater. Interfaces* **2018**, *10*, 37445–37452.

[11] Pathak, R.; Chen, K.; Gurung, A.; Reza, K. M.; Bahrami, B.; Pokharel, J.; Baniya, A.; He, W.; Wu, F.; Zhou, Y. et al. Fluorinated hybrid solid-electrolyte-interphase for dendrite-free lithium deposition. *Nat. Commun.* **2020**, *11*, 93.

[12] Aurbach, D.; Markovsky, B.; Weissman, I.; Levi, E.; Ein-Eli, Y. On the correlation between surface chemistry and performance of graphite negative electrodes for Li ion batteries. *Electrochim. Acta* **1999**, *45*, 67–86.

[13] Yu, P.; Haran, B. S.; Ritter, J. A.; White, R. E.; Popov, B. N. Palladium-microencapsulated graphite as the negative electrode in Li-ion cells. *J. Power Sources* **2000**, *91*, 107–117.

[14] Zhou, Z. P.; Zhang, H.; Zhou, Y.; Qiao, H.; Gurung, A.; Naderi, R.; Elbohy, H.; Smirnova, A. L.; Lu, H. T.; Chen, S. L. et al. Binder free hierarchical mesoporous carbon foam for high performance lithium ion battery. *Sci. Rep.* **2017**, *7*, 1440.

[15] Qu, X. L.; Zhang, X.; Gao, Y.; Hu, J. J.; Gao, M. X.; Pan, H. G.; Liu, Y. F. Remarkably improved cycling stability of boron-strengthened multicomponent layer protected micron-Si composite anode. *ACS Sustainable Chem. Eng.* **2019**, *7*, 19167–19175.

[16] Park, M. H.; Kim, M. G.; Joo, J.; Kim, K.; Kim, J.; Ahn, S.; Cui, Y.; Cho, J. Silicon nanotube battery anodes. *Nano Lett.* **2009**, *9*, 3844–3847.

[17] Chan, C. K.; Peng, H. L.; Liu, G.; McIlwrath, K.; Zhang, X. F.; Huggins, R. A.; Cui, Y. High-performance lithium battery anodes using silicon nanowires. *Nat. Nanotechnol.* **2008**, *3*, 31–35.

[18] Chen, X. L.; Gerasopoulos, K.; Guo, J. C.; Brown, A.; Wang, C. S.; Ghodssi, R.; Culver, J. N. Virus-enabled silicon anode for lithium-ion batteries. *ACS Nano* **2010**, *4*, 5366–5372.

[19] Liu, H. K.; Guo, Z. P.; Wang, J. Z.; Konstantinov, K. Si-based anode materials for lithium rechargeable batteries. *J. Mater. Chem.* **2010**, *20*, 10055–10057.

[20] Wang, W.; Kumta, P. N. Nanostructured hybrid silicon/carbon nanotube heterostructures: Reversible high-capacity lithium-ion anodes. *ACS Nano* **2010**, *4*, 2233–2241.

[21] Chen, X. L.; Gerasopoulos, K.; Guo, J. C.; Brown, A.; Ghodssi, R.; Culver, J. N.; Wang, C. S. High rate performance of virus enabled 3D n-type Si anodes for lithium-ion batteries. *Electrochim. Acta* **2011**, *56*, 5210–5213.

[22] Lee, S. J.; Lee, J. K.; Chung, S. H.; Lee, H. Y.; Lee, S. M.; Baik, H. K. Stress effect on cycle properties of the silicon thin-film anode. *J. Power Sources* **2001**, *97–98*, 191–193.

[23] Liu, Q.; Cui, Z.; Zou, R. J.; Zhang, J. H.; Xu, K. B.; Hu, J. Q. Surface coating constraint induced anisotropic swelling of silicon in Si-void@SiO_x nanowire anode for lithium-ion batteries. *Small* **2017**, *13*, 1603754.

[24] Li, W. H.; Sun, X. L.; Yu, Y. Si-, Ge-, Sn-based anode materials for lithium-ion batteries: From structure design to electrochemical performance. *Small Methods* **2017**, *1*, 1600037.

[25] Ashuri, M.; He, Q. R.; Shaw, L. L. Silicon as a potential anode material for Li-ion batteries: Where size, geometry and structure matter. *Nanoscale* **2016**, *8*, 74–103.

[26] Liu, N.; Wu, H.; McDowell, M. T.; Yao, Y.; Wang, C. M.; Cui, Y. A yolk-shell design for stabilized and scalable Li-ion battery alloy anodes. *Nano Lett.* **2012**, *12*, 3315–3321.

[27] Zhang, L.; Wang, C. R.; Dou, Y. H.; Cheng, N. Y.; Cui, D. D.; Du, Y.; Liu, P. R.; Al-Mamun, M.; Zhang, S. Q.; Zhao, H. J. A yolk-shell structured silicon anode with superior conductivity and high tap density for full lithium-ion batteries. *Angew. Chem., Int. Ed.* **2019**, *58*, 8824–8828.

[28] Pan, L.; Wang, H. B.; Gao, D. C.; Chen, S. Y.; Tan, L.; Li, L. Facile synthesis of yolk-shell structured Si-C nanocomposites as anodes for lithium-ion batteries. *Chem. Commun.* **2014**, *50*, 5878–5880.

[29] Li, B.; Qi, R. R.; Zai, J. T.; Du, F. H.; Xue, C.; Jin, Y.; Jin, C. Y.; Ma, Z. F.; Qian, X. F. Silica wastes to high-performance lithium storage materials: A rational designed Al_2O_3 coating assisted magnesiothermic process. *Small* **2016**, *12*, 5281–5287.

[30] Li, B.; Li, S. X.; Jin, Y.; Zai, J. T.; Chen, M.; Nazakat, A.; Zhan, P.; Huang, Y.; Qian, X. F. Porous Si@C ball-in-ball hollow spheres for lithium-ion capacitors with improved energy and power densities. *J. Mater. Chem. A* **2018**, *6*, 21098–21103.

[31] Liu, Y. J.; Tai, Z. X.; Zhou, T. F.; Sencadas, V.; Zhang, J.; Zhang, L.; Konstantinov, K.; Guo, Z. P.; Liu, H. K. An all-integrated anode via interlinked chemical bonding between double-shelled-yolk-structured silicon and binder for lithium-ion batteries. *Adv. Mater.* **2017**, *29*, 1703028.

[32] Xie, J.; Tong, L.; Su, L. W.; Xu, Y. W.; Wang, L. B.; Wang, Y. H. Core-shell yolk-shell Si@C@Void@C nanohybrids as advanced lithium ion battery anodes with good electronic conductivity and corrosion resistance. *J. Power Sources* **2017**, *342*, 529–536.

[33] Chandrasekaran, R.; Magasinski, A.; Yushin, G.; Fuller, T. F. Analysis of lithium insertion/deinsertion in a silicon electrode particle at room temperature. *J. Electrochem. Soc.* **2010**, *157*, A1139–A1151.

[34] Chen, M.; Li, B.; Liu, X. J.; Zhou, L.; Yao, L.; Zai, J. T.; Qian, X. F.; Yu, X. B. Boron-doped porous Si anode materials with high initial coulombic efficiency and long cycling stability. *J. Mater. Chem. A* **2018**, *6*, 3022–3027.

[35] Burton, L. C.; Madjid, A. H. Coulomb screening in intrinsic medium-gap semiconductors and the electrical conductivity of silicon at elevated temperatures. *Phys. Rev.* **1969**, *185*, 1127–1132.

[36] Kong, M. H.; Noh, J. H.; Byun, D. J.; Lee, J. K. Electrochemical characteristics of phosphorus doped silicon and graphite composite for the anode materials of lithium secondary batteries. *J. Electroceram.* **2009**, *23*, 376.

[37] Perego, M.; Bonafos, C.; Fanciulli, M. Phosphorus doping of ultra-small silicon nanocrystals. *Nanotechnology* **2010**, *21*, 025602.

[38] Liang, J. W.; Wei, D. H.; Lin, N.; Zhu, Y. C.; Li, X. N.; Zhang, J. J.; Fan, L.; Qian, Y. T. Low temperature chemical reduction of fusional sodium metasilicate nonahydrate into a honeycomb porous silicon nanostructure. *Chem. Commun.* **2014**, *50*, 6856–6859.

[39] Chen, S. Q.; Shen, L. F.; van Aken, P. A.; Maier, J.; Yu, Y. Dual-functionalized double carbon shells coated silicon nanoparticles for high performance lithium-ion batteries. *Adv. Mater.* **2017**, *29*, 1605650.

[40] Lu, Z. D.; Liu, N.; Lee, H. W.; Zhao, J.; Li, W. Y.; Li, Y. Z.; Cui, Y. Nonfilling carbon coating of porous silicon micrometer-sized particles for high-performance lithium battery anodes. *ACS Nano* **2015**, *9*, 2540–2547.

[41] Lv, G. X.; Zhu, B.; Li, X. Q.; Chen, C. L.; Li, J. L.; Jin, Y.; Hu, X. Z.; Zhu, J. Simultaneous perforation and doping of Si nanoparticles for lithium-ion battery anode. *ACS Appl. Mater. Interfaces* **2017**, *9*,

44452–44457.
[42] Nickel, N. H.; Lengsfeld, P.; Sieber, I. Raman spectroscopy of heavily doped polycrystalline silicon thin films. *Phys. Rev. B* **2000**, *61*, 15558–15561.
[43] Wei, W. S.; Xu, G. Y.; Wang, J. L.; Wang, T. M. Raman spectra of intrinsic and doped hydrogenated nanocrystalline silicon films. *Vacuum* **2007**, *81*, 656–662.
[44] Kim, J. S.; Choi, W.; Byun, D.; Lee, J. K. Electrochemical characteristics of phosphorus doped silicon for the anode material of lithium secondary batteries. *Solid State Ionics* **2012**, *212*, 43–46.
[45] Lu, P.; Mu, W. W.; Xu, J.; Zhang, X. W.; Zhang, W. P.; Li, W.; Xu, L.; Chen, K. J. Phosphorus doping in Si nanocrystals/SiO_2 multilayers and light emission with wavelength compatible for optical telecommunication. *Sci. Rep*. **2016**, *6*, 22888.
[46] Gao, X. J.; Guan, B.; Mesli, A.; Chen, K. X.; Dan, Y. P. Deep level transient spectroscopic investigation of phosphorus-doped silicon by self-assembled molecular monolayers. *Nat. Commun*. **2018**, *9*, 118.
[47] Huang, S. Q.; Cheong, L. Z.; Wang, D. Y.; Shen, C. Nanostructured phosphorus doped silicon/graphite composite as anode for high-performance lithium-ion batteries. *ACS Appl. Mater. Interfaces*. **2017**, *9*, 23672–23678.
[48] Dou, X. Y.; Chen, M.; Zai, J. T.; De, Z.; Dong, B. X.; Liu, X. J.; Ali, N.; Tsega, T. T.; Qi, R. R.; Qian, X. F. Carbon coated porous silicon flakes with high initial coulombic efficiency and long-term cycling stability for lithium ion batteries. *Sustainable Energy Fuels* **2019**, *3*, 2361–2365.
[49] Pollak, E.; Salitra, G.; Baranchugov, V.; Aurbach, D. *In situ* conductivity, impedance spectroscopy, and *ex situ* Raman spectra of amorphous silicon during the insertion/extraction of lithium. *J. Phys. Chem. C* **2007**, *111*, 11437–11444.
[50] Chen, K.; Pathak, R.; Gurung, A.; Adhamash, E. A.; Bahrami, B.; He, Q. Q.; Qiao, H.; Smirnova, A. L.; Wu, J. J.; Qiao, Q. Q. et al. Flower-shaped lithium nitride as a protective layer via facile plasma activation for stable lithium metal anodes. *Energy Storage Materials* **2019**, *18*, 389–396.
[51] Pathak, R.; Chen, K.; Gurung, A.; Reza, K. M.; Bahrami, B.; Wu, F.; Chaudhary, A.; Ghimire, N.; Zhou, B.; Zhang, W. H. et al. Ultrathin bilayer of graphite/SiO_2 as solid interface for reviving Li metal anode. *Adv. Energy Mater.* **2019**, *9*, 1901486.
[52] Su, L. W.; Xie, J.; Xu, Y. W.; Wang, L. B.; Wang, Y. H.; Ren, M. M. Preparation and lithium storage performance of yolk-shell Si@void@C nanocomposites. *Phys. Chem. Chem. Phys*. **2015**, *17*, 17562–17565.
[53] Han, Y.; Zou, J. D.; Li, Z.; Wang, W. Q.; Jie, Y.; Ma, J. M.; Tang, B.; Zhang, Q.; Cao, X.; Xu, S. M. et al. Si@void@C nanofibers fabricated using a self-powered electrospinning system for lithium-ion batteries. *ACS Nano* **2018**, *12*, 4835–4843.
[54] Jiang, J.; Zhang, H.; Zhu, J. H.; Li, L. P.; Liu, Y. N.; Meng, T.; Ma, L.; Xu, M. W.; Liu, J. P.; Li, C. M. Putting nanoarmors on yolk-shell Si@C nanoparticles: A reliable engineering way to build better Si-based anodes for Li-ion batteries. *ACS Appl. Mater. Interfaces* **2018**, *10*, 24157–24163.
[55] Nzabahimana, J.; Guo, S. T.; Hu, X. L. Facile synthesis of Si@void@C nanocomposites from low-cost microsized Si as anode materials for lithium-ion batteries. *Appl. Surf. Sci*. **2019**, *479*, 287–295.
[56] Celzard, A.; Marêché, J. F.; Payot, F.; Furdin, G. Electrical conductivity of carbonaceous powders. *Carbon* **2002**, *40*, 2801–2815.
[57] Pathak, R.; Gurung, A.; Elbohy, H.; Chen, K.; Reza, K. M.; Bahrami, B.; Mabrouk, S.; Ghimire, R.; Hummel, M.; Gu, Z. R. et al. Self-recovery in Li-metal hybrid lithium-ion batteries via WO_3 reduction. *Nanoscale* **2018**, *10*, 15956–15966.
[58] Li, Z. L.; Zhao, H. L.; Lv, P. P.; Zhang, Z. J.; Zhang, Y.; Du, Z. H.; Teng, Y. Q.; Zhao, L. N.; Zhu, Z. M. Watermelon-like structured SiO_x-TiO_2@C nanocomposite as a high-performance lithium-ion battery anode. *Adv. Funct. Mater.* **2018**, *28*, 1605711.
[59] Pathak, R.; Zhou, Y.; Qiao, Q. Q. Recent advances in lithiophilic porous framework toward dendrite-free lithium metal anode. *Appl. Sci.* **2020**, *10*, 4185.
[60] Li, B.; Xiao, Z. J.; Chen, M.; Huang, Z. Y.; Tie, X. Y.; Zai, J. T.; Qian, X. F. Rice husk-derived hybrid lithium-ion capacitors with ultra-high energy. *J. Mater. Chem. A* **2017**, *5*, 24502–24507.
[61] Li, B.; Dai, F.; Xiao, Q. F.; Yang, L.; Shen, J. M.; Zhang, C. M.; Cai, M. Nitrogen-doped activated carbon for a high energy hybrid supercapacitor. *Energy Environ. Sci.* **2016**, *9*, 102–106.
[62] Li, B.; Dai, F.; Xiao, Q. F.; Yang, L.; Shen, J. M.; Zhang, C. M.; Cai, M. Activated carbon from biomass transfer for high-energy density lithium-ion supercapacitors. *Adv. Energy Mater.* **2016**, *6*, 1600802.
[63] Liu, X. Y.; Jung, H. G.; Kim, S. O.; Choi, H. S.; Lee, S.; Moon, J. H.; Lee, J. K. Silicon/copper dome-patterned electrodes for high-performance hybrid supercapacitors. *Sci. Rep*. **2013**, *3*, 3183.
[64] Yi, R.; Chen, S. R.; Song, J. X.; Gordin, M. L.; Manivannan, A.; Wang, D. H. High-performance hybrid supercapacitor enabled by a high-rate Si-based anode. *Adv. Funct. Mater*. **2014**, *24*, 7433–7439.